Prediction of the anisotropic effective moduli of shales based on the Mori-Tanaka model and digital core technique

Zidong Wang[1], Gongqi Cao[1], Jianlin Liu[1, *], Li-Yun Fu[2, *]

[1] *College of Pipeline and Civil Engineering, China University of Petroleum (East China), Qingdao 266580, China*

[2] *College of Geosciences, China University of Petroleum (East China), Qingdao 266580, China*

* Corresponding author:

Jianlin Liu, E-mail: liujianlin@upc.edu.cn.

Li-Yun Fu, E-mail: lfu@upc.edu.cn.

Key Points:

- The Mori-Tanaka model and digital core technique are used to estimate the elastic properties of Longmaxi formation shale sample.
- The inclusions in shale have orientation law, which will affect the anisotropy of shale elastic properties.
- The anisotropic elastic of digital core predicted by Mori-Tanaka model and FEM are consistent.

Abstract

Natural rocks belong to the polymineral composite material with complex microstructures. Such a strong heterogeneity of rocks makes it difficult to estimate the effective moduli by traditional models in theory. In the present study, a Mori-Tanaka (MT) model considering the shape and orientation of inclusion minerals obtained by the micro-CT is established, and then it is applied to evaluate the anisotropic parameters of shales. In the MT model, the principal radii and Eulerian angles of the ellipsoidal inclusion are obtained by solving its inertia matrix through the micro-CT. According to these inclusion information, we make statistics on the ratio of average principal radii and the distribution of Eulerian angles of inclusions with different minerals. In what follows, the effective elastic stiffness matrix of shale samples is predicted by the MT model, and the corresponding digital core is input for finite element method (FEM) analysis to verify the accuracy of the theoretical results. It is shown that the anisotropy of the elastic stiffness matrix predicted by the MT model and FEM is consistent under two sizes of representative volume elements. These findings are potential for applications in rock mechanics, civil engineering and oil exploitation, etc.

Plain Language Summary

The elastic properties and anisotropy of reservoir rock is of great significance for reservoir exploration and drilling, which are associated with complex micro-structures and strong heterogeneity. The rock physics model especially effective medium is of great significance for the prediction of rock elastic. Mori-Tanaka (MT) model is one of the most widely used method to evaluate the elastic properties of material with complex shape and orientation inclusions. In order to make the MT model more practical, the information of different inclusions in shale

sample are obtained by micro-CT and digital core. And the ellipsoidal inclusions required in the MT model are approximated by calculating the moment of inertia of irregular inclusions. Therefore, in this study, the elastic stiffness matrix of shale containing kinds of inclusions that can reflect the anisotropy of elastic properties are predicted by the MT model considering the shape and orientation of representative ellipsoidal inclusions. Finally, we found that the effective modulus of shale is anisotropic by the MT model, and verified the anisotropy law predicted by the MT model and the finite element method. The anisotropy in shale is mainly caused by the non-random arrangement of pores, TOC and clay.

Keywords: Mori-Tanaka model; digital core; numerical simulation; effective modulus; anisotropy

1 Introduction

The unconventional reservoir rocks, such as the tight sandstone and shale, are characteristic of multi-mineral compositions and complex microstructures. The resulting strong heterogeneity and complex mechanical properties challenge the evaluation to predict the overall elastic properties of reservoir rocks (Prasad & Pal-Bathijia, 2009; Jian et al., 2020). Particularly, the directionally distributed pores or other minerals in tight sandstones or shales from deep reservoirs as deviatoric stress fields often make reservoir rocks be anisotropic, and this fact significantly increases the difficulty to estimate effective moduli by conventional models in theory (Shapiro & Kaselow, 2005; Gui et al., 2018; Zhang et al., 2020).

To consider the anisotropy of reservoir rocks, many models have been proposed (Vernik & Nur, 1992; Hudson, 1986; Cheng, 1993), but the consideration of the shape and orientation of minerals is missing. In practice, the theory of mesomechanics starting from the Eshelby

tensor (Eshelby, 1957) has been extensively applied in composite materials (Berryman, 1995; Raju et al., 2018), among which the Mori-Tanaka (MT) model (Mori & Tanaka, 1974) is one of the most representative methods (Park et al., 2020) and it has been applied in many fields00(Shen and Wang, 2012; Wang et al., 2017). Zimmerman & David (1991, 2011a, 2011b) has systematically analyzed many effective medium models including the MT model, and deduced the pore's compressibility and shear compliance, which has greatly promoted the application of MT model in rock physics. In succession, Deng et al. (2015) use the MT model to calculate the effective moduli of a dry sandstone containing randomly distributed spherical inclusions. Goodarzi et al. (2016) compared the applicability of MT, self-consistent and generalized self-consistent models in evaluating the effective moduli of shale, and they found the MT and generalized self-consistent models can accurately predict the bulk modulus. Similarly, Zhao et al. (2018) compared the shale moduli predicted by the MT and self-consistent models based on the micro indentation results, and it was claimed that the MT model can better predict the anisotropy of shales.

Although the MT model has been introduced into the evaluation of the elastic properties of shales, the shape and orientation of inclusions in the MT model are assumed theoretically in previous studies. With the development of micro-computed tomography (micro-CT) and digital core technologies (2019), it is now possible to introduce the real information of inclusions in shales into the MT and other theoretical models. The micro-CT has been widely used to predict the effective moduli of composites (Sahimi & Tahmasebi, 2021), and the digital core technique is effectively used to describe the porous media in the analysis of rock conductivity, heat conduction and seepage (Zhao et al., 2020). In terms of elastic properties of rocks, the finite element method (FEM) is a most conventional tool to analyze the digital core, which is accurate but time-consuming. However, there are few investigations on the application of digital core

to effective medium models including the MT model to evaluate the elastic properties of shales.

For combination of the MT model and the digital core technique, the key point is how to extract the geometric parameters of inclusions required in the Eshelby tensor. Drach et al. (2011, 2013) developed a method to extract individual pore inclusions from the micro-CT data, and classified the irregular characteristic groups by using the moment of inertia of any irregularly shaped pores. Park et al. (2020) obtained the distribution laws of pore shape and orientation in AE cement by the pore's inertia matrix, and predicted the effective moduli of anisotropic AE cement by the MT model. Considering that the inclusions with small stiffness such as pores and clay in the shale have similar laws, Giraud et al. (2007) proposed a theoretical model to describe the orientation distribution of inclusions. However, there are few studies on applying the inclusion's inertia matrix obtained by the micro-CT to the evaluation of shale's elastic properties.

The direct goal of this study is to obtain the inertia matrix of inclusions in the shale through the micro-CT, in order to analyze the shape and orientation laws of different kind of inclusions. This information on the inclusions is combined with the Mori-Tanaka model to evaluate the anisotropic properties of shale sample and the contribution of different kinds of inclusions. The outline of this article is organized as follows. In section 2, the principle of MT model to predict the anisotropy of shale's elastic properties is introduced, which the definition and introduction of Eulerian angles are formulated. In section 3, through the reconstruction of CT images of the shale sample in Longmaxi formation, the shape and orientation information of inclusions with different components are obtained and analyzed. In section 4, the elastic stiffness matrix of the shale sample is quantified by the MT model, and the effect of different kinds of inclusions to the shale's anisotropy is discussed. Moreover, a comparison of the results by the MT model and FEM analysis is presented to verify the accuracy of the MT model in predicting the

anisotropic properties of shales.

2 Fundamentals of the MT model considering the inclusion's orientation

We first give the illustration of the Mori–Tanaka model, which is one of the most widely used methods to predict the effective properties of composite materials in various fields. The interaction among inclusions can be considered by distinguishing the far-field strain and the matrix strain in the MT model, so it is suitable for the analysis of representative volume element (RVE) including large volume fraction inclusions. For the shale with multiple and morphological inclusions, the prediction formulas of the effective modulus can be expressed as (Shen et al., 2013)

$$\bar{\boldsymbol{C}}=\boldsymbol{C}_0+\sum_{r=1}^{N-1} f_r\left[\left(\boldsymbol{C}_r-\boldsymbol{C}_0\right)^{-1}+f_0\boldsymbol{S}_r\boldsymbol{C}_0^{-1}\right]^{-1}, \tag{1}$$

where $\bar{\boldsymbol{C}}$ is the effective elastic stiffness tensor, $\boldsymbol{C}_0$ represents the elastic stiffness of matrix, and N is the number of components in the shale including the matrix and (N–1) kinds of inclusions. The subscript r is the component number, where 0 corresponds to the matrix. The parameter f_r is the volume fraction of each component, satisfying $\sum_{r=0}^{N-1} f_r=1$. The quantity $\boldsymbol{C}_r$ is the elastic stiffness tensor of the r-th component, and $\boldsymbol{S}_r$ is the Eshelby tensor of the r-th component, satisfying $\boldsymbol{S}_r = \boldsymbol{P}_r\boldsymbol{C}_0$. The expression of the Hill tensor $\boldsymbol{P}_r$ of general ellipsoidal inclusions is listed in Appendix A.

In the prediction of effective modulus using the MT model, each inclusion can be regarded as an ellipsoid, and the three principal radii of an ellipsoidal inclusion satisfy $a_1>a_2>a_3$, i.e. the principal inertia of the ellipsoid satisfies $M_{11}< M_{22}< M_{33}$. The orientation of the ellipsoid with

principal axes O-$x_1x_2x_3$ with respect to a set of axes O-XYZ fixed in the shale may be specified by the three Eulerian angles ψ, θ and φ. The process is that the principal coordinate O-$x_1x_2x_3$ of any orientation in space can be obtained by three rotations of the axes O-XYZ and the specific process is schematized in Figure 1.

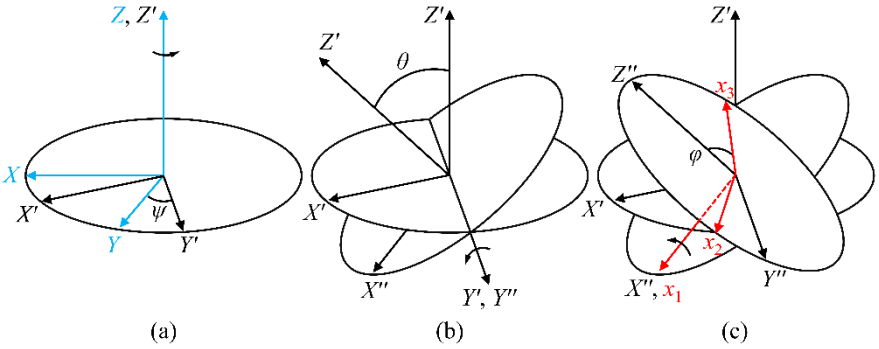

Figure 1. Schematic transformation of the Eulerian angles

Therefore, for any fourth-order tensor expressed as $\boldsymbol{A}'$ in the axes O-$x_1x_2x_3$, its form $\boldsymbol{A}$ in the axes O-XYZ can be derived by the transformation equation, which is

$$\boldsymbol{A}=\boldsymbol{T}^{-1}\boldsymbol{A}'\boldsymbol{T}, \tag{2}$$

where $\boldsymbol{T}$ is a fourth order transformation tensor, and its corresponding 6×6 matrix form is

$$[\boldsymbol{T}]=\begin{bmatrix}\boldsymbol{T}_1 & 2\boldsymbol{T}_2\\ \boldsymbol{T}_3 & \boldsymbol{T}_4\end{bmatrix},$$

$$[\boldsymbol{T}_1]=\begin{bmatrix}R_{11}^2 & R_{21}^2 & R_{31}^2\\ R_{12}^2 & R_{22}^2 & R_{32}^2\\ R_{13}^2 & R_{23}^2 & R_{33}^2\end{bmatrix}, \tag{3}$$

$$[\boldsymbol{T}_2]=\begin{bmatrix}R_{21}R_{31} & R_{31}R_{11} & R_{11}R_{21}\\ R_{22}R_{32} & R_{32}R_{12} & R_{12}R_{22}\\ R_{23}R_{33} & R_{33}R_{13} & R_{13}R_{23}\end{bmatrix},$$

$$[\boldsymbol{T}_3]=\begin{bmatrix} R_{12}R_{13} & R_{22}R_{23} & R_{32}R_{33} \\ R_{13}R_{11} & R_{23}R_{21} & R_{33}R_{31} \\ R_{11}R_{12} & R_{21}R_{22} & R_{31}R_{32} \end{bmatrix},$$

$$[\boldsymbol{T}_4]=\begin{bmatrix} R_{22}R_{33}+R_{23}R_{32} & R_{32}R_{13}+R_{33}R_{12} & R_{12}R_{23}+R_{13}R_{22} \\ R_{23}R_{31}+R_{21}R_{33} & R_{33}R_{11}+R_{31}R_{13} & R_{13}R_{21}+R_{11}R_{23} \\ R_{21}R_{32}+R_{22}R_{31} & R_{31}R_{12}+R_{32}R_{11} & R_{11}R_{22}+R_{12}R_{21} \end{bmatrix}.$$

The symbol R_{kl} represents the component of a second-order tensor $\boldsymbol{R}$ in its 3×3 matrix form, which reads

$$[\boldsymbol{R}]=[\boldsymbol{R}_\psi \boldsymbol{R}_\theta \boldsymbol{R}_\varphi]=\begin{bmatrix} R_{11} & R_{12} & R_{13} \\ R_{21} & R_{22} & R_{23} \\ R_{31} & R_{32} & R_{33} \end{bmatrix}, \tag{4}$$

where $\boldsymbol{R}_\psi$, $\boldsymbol{R}_\theta$ and $\boldsymbol{R}_\varphi$ correspond to the second-order tensors of ψ, θ and φ to transform the vector from axes O-$x_1x_2x_3$ to axes O-XYZ, which are written as

$$[\boldsymbol{R}_\psi]=\begin{bmatrix} \cos\psi & -\sin\psi & 0 \\ \sin\psi & \cos\psi & 0 \\ 0 & 0 & 1 \end{bmatrix},$$

$$[\boldsymbol{R}_\theta]=\begin{bmatrix} \cos\theta & 0 & \sin\theta \\ 0 & 1 & 0 \\ -\sin\theta & 0 & \cos\theta \end{bmatrix}, \tag{5}$$

$$[\boldsymbol{R}_\varphi]=\begin{bmatrix} 1 & 0 & 0 \\ 0 & \cos\varphi & -\sin\varphi \\ 0 & \sin\varphi & \cos\varphi \end{bmatrix}.$$

Then, the matrix form of $\boldsymbol{R}$ is

$$[\boldsymbol{R}]=\begin{bmatrix} \cos\psi\cos\theta\cos\varphi-\sin\psi\sin\varphi & \sin\psi\cos\theta\cos\varphi+\cos\psi\sin\varphi & -\sin\theta\cos\varphi \\ \cos\psi\cos\theta\sin\varphi-\sin\psi\cos\varphi & -\sin\psi\cos\theta\sin\varphi+\cos\psi\cos\varphi & \sin\theta\sin\varphi \\ \cos\psi\sin\theta & \sin\psi\sin\theta & \cos\theta \end{bmatrix}. \quad (6)$$

When considering the orientation of inclusions, Equation (1) can be recast as

$$\bar{\boldsymbol{C}}=\boldsymbol{C}_0+\sum_{r=1}^{N-1}\sum_{i=1}^{n_r} f_{r,i}\left\{\boldsymbol{T}_{r,i}^{-1}\left[\left(\boldsymbol{C}_{r,i}-\boldsymbol{C}_0\right)^{-1}+f_0\boldsymbol{S}_{r,i}\boldsymbol{C}_0^{-1}\right]^{-1}\boldsymbol{T}_{r,i}\right\}, \quad (7)$$

where n_r represents the total number of inclusions of the r-th component, the subscript i is the inclusion number, the subscript (r,i) represents the i-th inclusion in the r-th component, and $\boldsymbol{T}_{r,i}$, $\boldsymbol{C}_{r,i}$ and $\boldsymbol{S}_{r,i}$ are the corresponding transformation tensor, elastic stiffness tensor and Eshelby tensor, respectively.

On the premise that geometric parameters are obtained, the effective elastic stiffness tensor of the shale can be predicted by MT model according to Equation (7). The shape and orientation parameters of all inclusions will be detemined in Section 3.

3 Image processing and component information statistics

3.1 Digital core of the Longmaxi formation shale

Next, the core sample of the Longmaxi formation shale with a diameter of about 4 mm is used to generate the so-called digital core. The core is tomographed by Shanghai Synchrotron Radiation CT Facility from Shanghai Institute of Applied Physics, Chinese Academy of Sciences. Based on the different absorption capacity of different substances to light, a set of 1397 high-resolution core slice images are obtained, which represent different components by different gray levels. Figure 2 shows that the first and last horizontal slice images of this core, and each image contains 2000×1400 pixels. Different components of the shale can be clearly distinguished according to different gray levels of the image, such as pores and TOC (the

darkest part, shown in yellow circles), pyrite (shown in white and red circles), clay, quartz, feldspar and other minerals (gray black to gray white, shown in blue and green boxes). It can be seen that the shale of Longmaxi demonstrates a very strong heterogeneity, which has a major impact on the elastic properties and anisotropy of the rock. Specifically, the directional arrangement of pores and clays in the shale may lead to the obvious anisotropy (Sayers, 1994).

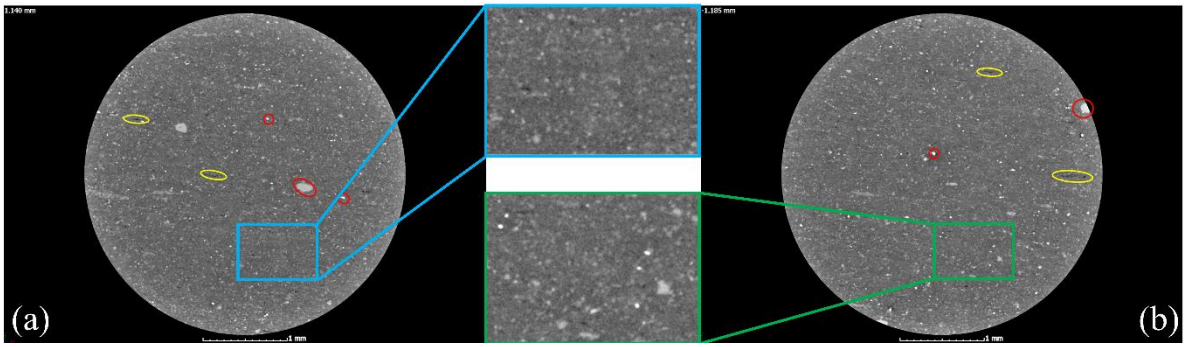

Figure 2. Horizontal slices of the Longmaxi formation shale's digital core images, where (a) is the first horizontal slice image; (b) the last (1397th) horizontal slice image.

For the subsequent analysis of the shale's effective modulus, it is necessary to batch preprocess the images and divide the core into six components according to the gray level, which are (1) pore, (2) TOC, (3) clay, (4) quartz, (5) feldspar, calcite, and (6) pyrite, siderite (Jian et al. 2020). The preprocessed image is divided into six relatively fixed gray values, and the first and last preprocessed images are shown in Figure 3. It is more clearly to distinguish the different components, and the difficulty of 3D reconstruction is reduced.

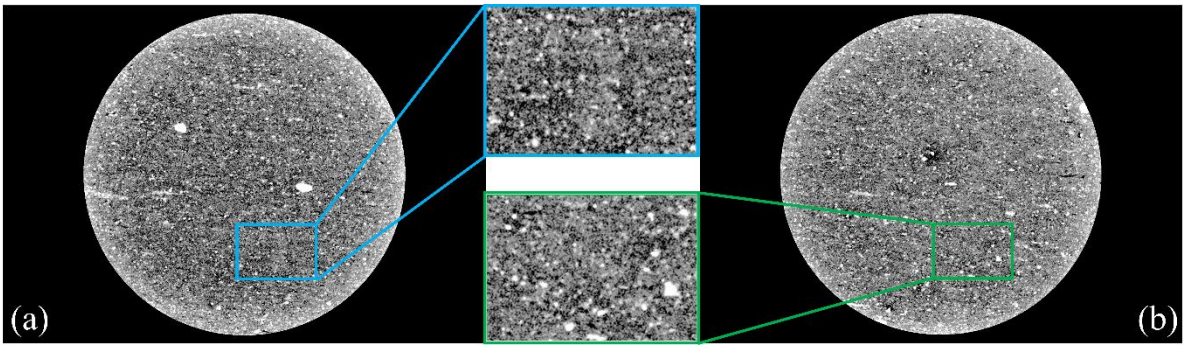

Figure 3. Horizontal slices after multi threshold segmentation, where (a) is the first horizontal slice image and (b) is the last (1397th) horizontal slice image.

Then, all the slice images are imported for 3D reconstruction. Based on the results of computed tomography, we determine that the sizes of a pixel are 2.841 μm, 2.841 μm and 1.665 μm along *X*, *Y* and *Z*-axes, respectively. The reconstructed core of the scanning section is shown in Figure 4 (a). However, the cylindrical core cannot meet the boundary symmetry conditions required for the RVE analysis, so the cuboid containing 900×900×1200 pixels is intercepted from the core center and marked as RVE_{total}, as shown in Figure 4 (b).

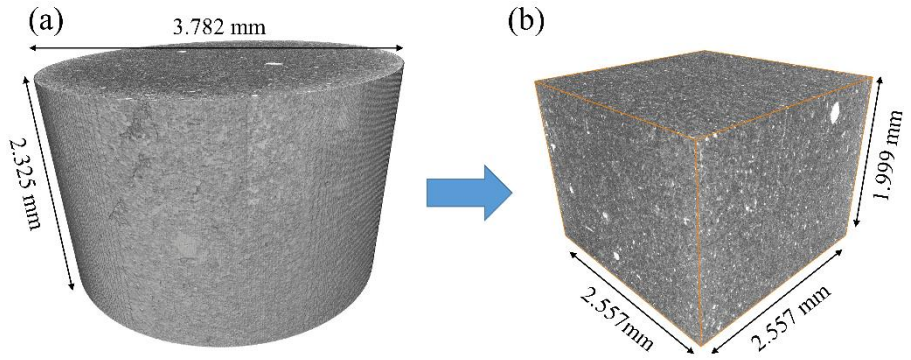

Figure 4. 3-D reconstruction of shale digital core in the Longmaxi formation, where (a) sample of scanning section; (b) RVE_{total} for analysis.

3.2 Geometric information of each component

Binarization is carried out to obtain the corresponding components in RVE_{total} by setting different thresholds, and the binarization results of pores are shown in Figure 5 (a). In fact, the RVE_{total} in Figure 5 (a) contains more than 10^5 individual pore inclusions, which is a huge task for mesh generation. In addition, we take a single pore inclusion from the RVE_{total}, which is displayed in Figures 5 (b) to (d). It can be found that the pores obtained only by threshold segmentation has the irregular and sharp boundaries in Figures 5 (c) and (d). These defects and bulges have little effect on the anisotropy of the shale caused by pores, but they will greatly affect the calculation efficiency of the MT model and FEM. Therefore, we have carried out the digital image processing on the core, and the process includes removing small holes, segmentation, closing, opening, and removing small spots and median filtering. The processed results of pores in the RVE are demonstrated in Figures 5 (e) to (h). It can be seen from Figure 5 (e) that the small volume pores are deleted and the number of pores decreases significantly. On the premise of maintaining the overall characteristics of pores, the opening and closing operation can reduce the defects and bulges of pores, which can be obtained by comparing Figures 5 (c), (d) and (g), (h).

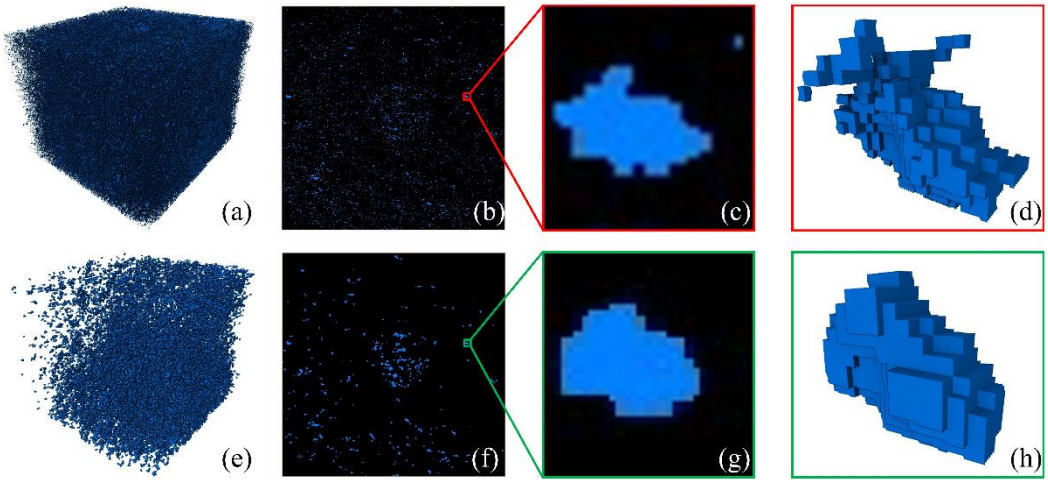

Figure 5 Comparison between pores inclusions before and after image processing, where (a), (b), (c) and (d) are the figures before the image processing, and (e), (f), (g) and (h) are the figures after the image processing, respectively. Figures (a) and (e) are the pore inclusions in the RVE; (b) and (f) are the horizontal slice images of pore inclusions; (c) and (g) show a horizontal slice of an isolated pore; (d) and (h) are the corresponding 3-D reconstructed pores.

By adjusting the relevant parameters in the image processing, the volume fraction of each component before and after processing is maintained at a similar value. The volume fraction of each component after processing is shown in Table 1. It can be seen from Table 1 that the component with the largest volume fraction in the RVE is quartz, which exceeds 50%, so it should be used as the matrix phase when using the MT model. Accordingly, other components are considered as inclusions. In addition, the bulk and shear moduli of each component are listed in Table 1.

Table 1 Elastic paramaters and volume fractions of different mineral components (Mavko et al., 1998)

Number	Mineral phase	Bulk modulus (GPa)	Shear Modulus (GPa)	Volume fraction
0	Quartz	37	44	0.5411
1	Pores	2.25	0.001	0.0328
2	TOC	2.9	2.7	0.0481
3	Clay	20.9	6.85	0.2873
4	Feldspar	71.998	34.978	0.0759
5	Pyrite	134.685	102.704	0.0148

3.3 Ellipsoidal approximation of inclusions

Inclusions of different components in the shale usually have irregular shapes. For example, the pores in Figure 5 (h) show a kind of shape similar to a flat ellipsoid. However, the ellipsoid is usually adopted as a representative shape to characterize the contribution of inclusion to the RVE's mechanical properties in mesomechanics (Drach et al., 2011), and so is the MT model. In a previous study, Drach et al. used the moment of inertia of the pore to classify the irregular pores of carbon/carbon composites, and it was verified that the inertia matrix of the inclusion can significantly affect the anisotropy of the RVE (Drach et al., 2013). As a consequence, the principal radius and principal direction of the approximate ellipsoidal inclusion used in the MT model are obtained through the inertia matrix of the irregular inclusion.

The inertia matrix of an irregular shaped inclusion in the coordinate system *O-XYZ* is

$$[\boldsymbol{I}]=\begin{bmatrix} I_{XX} & I_{XY} & I_{XZ} \\ I_{YX} & I_{YY} & I_{YZ} \\ I_{ZX} & I_{ZY} & I_{ZZ} \end{bmatrix}=m\begin{bmatrix} M_{2Y}+M_{2Z} & -M_{2XY} & -M_{2XZ} \\ -M_{2XY} & M_{2X}+M_{2Z} & -M_{2YZ} \\ -M_{2XZ} & -M_{2YZ} & M_{2X}+M_{2Y} \end{bmatrix}, \tag{8}$$

where $\boldsymbol{I}$ is the inertia tensor of the irregular shaped inclusion, [$\boldsymbol{I}$] is the corresponding inertia matrix, I_{XX}, I_{YY}, I_{ZZ} are the moments of inertia of the inclusion along *X*, *Y*, and *Z* directions, respectively, and I_{XY}, I_{YZ}, I_{ZX} are the inertia products of the inclusion in the *X*-*Y*, *Y*-*Z*, and *Z*-*X* planes, respectively, *m* is the mass of the inclusion, and M_{2X}、M_{2Y}、M_{2Z}、M_{2XY}、M_{2YZ}、M_{2ZX} is detailed in Appendix B.

After establishing the inertia matrix of the inclusion, the principal moment of inertia and the direction of the principal axes can be obtained. Then, the principal radii of the approximate ellipsoidal inclusions can be obtained according to Equation (8) and the Eulerian angles corresponding to the principal axes of each inclusion can be obtained by using the dcm2angle function in MATLAB via the relations

$$a_1=\sqrt{\frac{5}{2}\left(I_2+I_3-I_1\right)},\quad a_2=\sqrt{\frac{5}{2}\left(I_1+I_3-I_2\right)},\quad a_3=\sqrt{\frac{5}{2}\left(I_1+I_2-I_3\right)}, \tag{9}$$

where I_1, I_2, I_3 are the first, second and third principal moments of inertia of the inclusion respectively.

3.3 Statistics of shape and orientation information of inclusions

Previous results show that the shape and orientation of inclusions will significantly affect the elastic properties and anisotropy of the shale. Generally, when the effective medium model

is used for calculation, the inclusion is considered as a rotating ellipsoid, that is, $a_1 = a_2$ or $a_2 = a_3$. The aspect ratio α is used to describe the shape of rotating ellipsoidal inclusion. Since the size relationship between the three principal radii is defined in this study, there are two cases for the value of α: (1) when $a_1 = a_2$, $\alpha = a_3/a_1 < 1$; (2) when $a_2 = a_3$, $\alpha = a_1/a_3 > 1$. Previous studies have mostly discussed the influence of the aspect ratio of the inclusion on the elastic properties of the rock, but the selection of the aspect ratio of the inclusion is mostly assumed in advance. Therefore, extracting the shape information of components in the shale by the digital core technology and making reasonable ellipsoid approximation are of a certain significance for the selection of aspect ratio.

The average principal radii of all inclusions in different components are counted to determine the representative shapes of inclusions in different components, which can be obtained by

$$\bar{a}_{1,r} = \sum_{i=1}^{n_r} \frac{a_{1,i} V_i}{V_r}, \quad \bar{a}_{2,r} = \sum_{i=1}^{n_r} \frac{a_{2,i} V_i}{V_r}, \quad \bar{a}_{3,r} = \sum_{i=1}^{n_r} \frac{a_{3,i} V_i}{V_r}, \tag{10}$$

where $\bar{a}_{1,r}$, $\bar{a}_{2,r}$ and $\bar{a}_{3,r}$ are the first, second and third average principal radii of the r-th component, respectively, $a_{1,i}$, $a_{2,i}$ and $a_{3,i}$ are the first, second and third principal radii of the i-th inclusion, V_i is the volume of the i-th inclusion, and V_r is the total volume of the component r.

Since the Hill tensor of an ellipsoidal inclusion is only related to the ratio between the principal radii and is independent of its size, the two ratios ($\bar{a}_2 / \bar{a}_1$ and $\bar{a}_3 / \bar{a}_1$) of each inclusion are the shape parameters affecting the calculation results of the MT model. The values $\bar{a}_2 / \bar{a}_1$ and $\bar{a}_3 / \bar{a}_1$ of five components are shown in Figure 6. The two ratios of inclusions can

be divided into four cases: (1) When $\bar{a}_2/\bar{a}_1$, $\bar{a}_3/\bar{a}_1 \to 1$, the inclusions tend to take the spherical shape; (2) When $\bar{a}_2/\bar{a}_1 \to 1$, $\bar{a}_3/\bar{a}_1 \ll 1$, the inclusions tend to take the disk shape; (3) When $\bar{a}_2/\bar{a}_1$, $\bar{a}_3/\bar{a}_1 \ll 1$, the inclusions tend to take the needle shape; (4) When $0 \ll \bar{a}_2/\bar{a}_1 \ll \bar{a}_3/\bar{a}_1 \ll 1$, the inclusions are the general ellipsoids without obvious characteristics. It can be seen from Figure 6 that, in the shale samples, the clay, feldspar and pyrite tend to be the needle shape, while the pores and TOC show general ellipsoids without obvious characteristics.

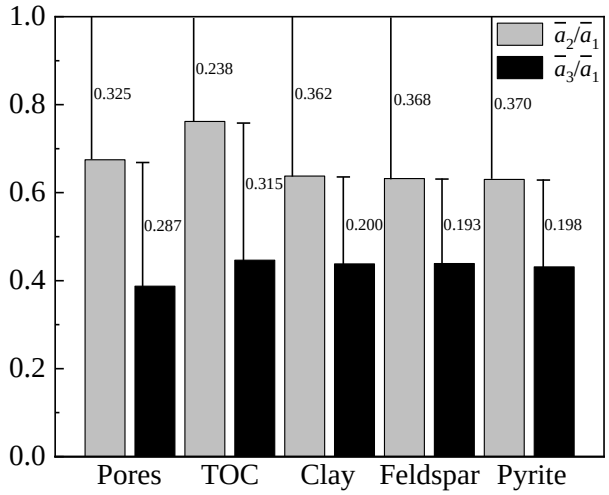

Figure 6 Ratio of average principal radii of inclusions with different components

Similarly, the Eulerian angles of inclusions with different components are statistically analyzed, where we take the pores as an example. The Eulerian angle distributions of the pore inclusions are shown in Figure 7. As can be seen from Figure 7, there is a large pore with the volume of 1.315×10^8 μm^3 in the digital core, which accounts for 30.661% of the total pore's volume. If the influence of the maximum pore on the law is ignored, it can be seen from the orientation distribution that ψ, θ and φ tend to the maximum at 0 degrees. From the orientation distribution of the three Eulerian angles, ψ has obvious symmetry, while the distributions of θ

and φ are not regular.

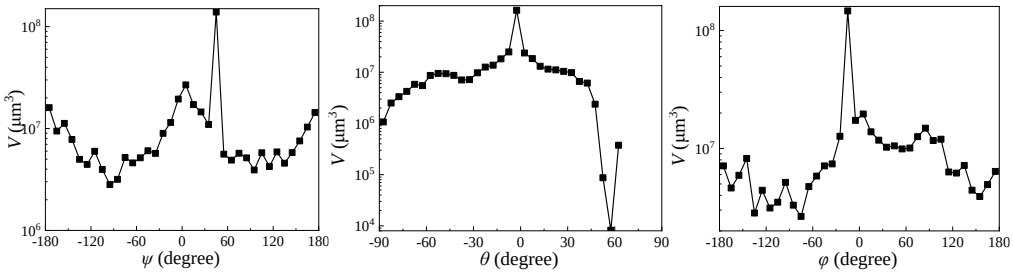

Figure 7 Euler angle distribution of pores inclusions in RVE_{total}

It is very interesting that the distribution law of ψ is similar to the theoretical model given by Giraud, et al. (2007) to describe the orientation distribution function of inclusions in rocks, which can be expressed as

$$W(\psi) = \frac{\sigma \cosh(\sigma \cos\psi)}{\sinh \sigma}, \tag{11}$$

where $W(\psi)$ is the orientation distribution function of ψ, σ is the parameter for the degree of the preferred alignment.

There are two typical distribution orientation cases: (1) When $\sigma \to 0$, the distribution of ψ of inclusions is uniform; (2) When $\sigma \to \infty$, the inclusions of the r-th component have the same ψ. In other words, the effect of inclusions on the anisotropy of materials increases with the increase of σ. Therefore, the parameter σ can be used to describe the degree of anisotropy of orientation distribution. The orientation distribution functions of the five kinds of components can be fitted by Equation (8), and the fitting results are shown in Figure 8. The value of σ of five components inclusions in the sample core are TOC, clay, pore, pyrite and feldspar from large to small. This means that, when just considering the orientation distribution, the TOC, clay and pores have more obvious effects on the anisotropy of the sample core,

followed by the pyrite, and the feldspar has no contribution to the anisotropy of the sample core due to its $\sigma = 0$.

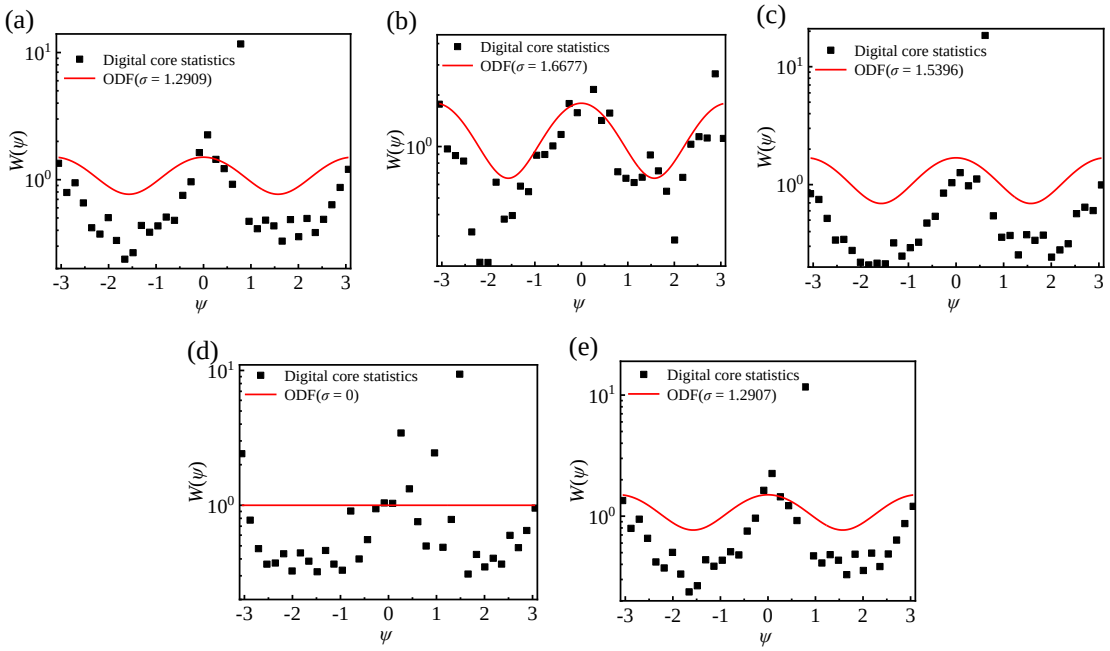

Figure 8 Orientation distribution function of inclusions with different components, where (a) pores, (b) TOC, (c) clay, (d) feldspar and (e) pyrite.

4 Results comparison of the MT model and FEM

4.1 Effective moduli of the shale sample predicted by the MT model

In this section, the anisotropic effective moduli of the shale sample (RVE_{total}) is predicted by using Equation (7) and the inclusion information in section 3.3. The volume fraction of each component inclusion (f_r) is taken in Table 1, and the volume fraction of matrix/quartz (f_0) is $f_0 = 1 - \sum_{r=1}^{N-1} f_r$. When analyzing the effect of each component to anisotropy of RVE_{total}, the RVE_{total} is considered as a two-phase material, and thus $f_0 = 1 - f_r$.

The components of the effective elastic stiffness matrix of RVE predicted by the MT

model are shown in Table 2. From the prediction results of C_{11}, C_{22} and C_{33}, it can be seen that the pores, TOC and clay contribute greater to the anisotropy of the shale sample than the feldspar and pyrite. Moreover, the results of the pores, TOC and clay on the anisotropy is same, that is, $C_{11}>C_{22}>C_{33}$ and $C_{44}<C_{55}<C_{66}$, and their differences between C_{11} and C_{33} are 2.466 GPa, 2.860 GPa and 2.844GPa, respectively. However, the results of the feldspar and pyrite are $C_{22}>C_{11}>C_{33}$, $C_{44}<C_{66}<C_{55}$ and $C_{11}>C_{33}>C_{22}$, $C_{44}<C_{66}<C_{55}$, and their differences between C_{11} and C_{33} are only 0.014 GPa and 0.069 GPa, respectively.

Actually, different components with different moduli will take different distribution forms under the action of in-situ stress, which directly reflects their contributions to the anisotropy of the shale. For example, the moduli of pores, TOC and clay are generally smaller than that of the quartz/matrix, so their contributions are similar. The moduli of the feldspar are similar to that of the quartz/matrix, and the moduli of the pyrite are significantly larger than that of the quartz/matrix, so their contributions are different.

The components of the elastic stiffness matrix of RVE_{total} containing five kinds of inclusions predicted by the MT model are shown in Table 2. The anisotropy laws of this RVE_{total} are $C_{11}>C_{22}>C_{33}$ and $C_{44}<C_{55}<C_{66}$, which are mainly affected by the internal pores, TOC and clay. The difference between C_{11} and C_{33} is 3.299 GPa, and the Thomsen anisotropy coefficients (Thomsen, 1986) ε and γ are 0.0259 and 0.0175, respectively, which shows that the anisotropy of this sample is still relatively small. However, as a preliminary attempt, it is of significance to analyze the rationality of the MT model in the prediction of the shale's effective moduli.

Table 2 Effective elastic stiffness matrix of RVE_{total} predicted by MT model (GPa)

Inclusion type	Quartz matrix					
	Pores	TOC	Clay	Feldspar	Pyrite	All type of inclusions

C_{11}	90.645	89.169	71.320	96.631	97.210	66.911
C_{12}	7.491	7.460	12.139	10.167	8.042	14.210
C_{13}	7.534	7.598	12.623	10.124	8.064	14.525
C_{22}	89.666	88.547	70.166	96.671	97.016	65.581
C_{23}	7.541	7.615	12.952	10.152	8.033	14.696
C_{33}	88.179	86.309	68.476	96.617	97.141	63.612
C_{44}	81.642	80.027	56.796	86.489	89.049	50.170
C_{55}	81.958	80.177	57.109	86.495	89.105	50.536
C_{66}	82.720	81.389	58.497	86.490	89.048	51.930

4.2 Validation by FEM

Although the influence of the shape and orientation of inclusions on the effective modulus of materials is considered in the MT model, there are still two following reasons which may cause the prediction errors. The first is that, the shape of the inclusion is simplified as an ellipsoid, which may cause the variation of the matrix's stress distribution around the inclusion and affect the prediction results. The other is that, in the effective medium models including the MT model, the location of inclusions in the RVE cannot be considered, and the inclusions with an obvious regular arrangement may also effect the anisotropy of materials. As a result, the accuracy of the MT model in predicting the effective moduli and anisotropy of RVE is verified by FEM using ABAQUS.

It should be noted that the geometry of the RVE obtained in Section 3.2 needs to be

meshed, which means the amount of calculation using FEM is much greater than that using the MT model. There are tens of thousands of inclusions in the RVE_{total} and it is unrealistic to analyze directly by FEM. Therefore, the RVE_{total} is divided into 36 RVEs containing 300×300×300 pixels and numbered as RVE_1 to RVE_{36} for subsequent analyses.

In order to facilitate comparison, the analysis object is taken as the quartz-pore material. The moduli of the quartz and saturated pores are shown in Table 1. The deformation of the generated quartz/matrix mesh is consistent with that of the pore/inclusion mesh, that is, the boundaries of the two kinds of meshes are the consistent pair. In addition, both the quartz/matrix and pores/inclusions are reconstructed by tetrahedral grids. By adding the Micromechanics Plug-ins modulus into ABAQUS, the following strains known as the Lagrangian strains (Moon et al., 2015), are applied to the RVE:

$$\varepsilon_1=\begin{bmatrix}1&0&0\\0&0&0\\0&0&0\end{bmatrix},\ \varepsilon_2=\begin{bmatrix}0&0&0\\0&1&0\\0&0&0\end{bmatrix},\ \varepsilon_3=\begin{bmatrix}0&0&0\\0&0&0\\0&0&1\end{bmatrix},$$
$$\varepsilon_4=\begin{bmatrix}0&0&0\\0&0&0.5\\0&0.5&0\end{bmatrix},\ \varepsilon_5=\begin{bmatrix}0&0&0.5\\0&0&0\\0.5&0&0\end{bmatrix},\ \varepsilon_6=\begin{bmatrix}0&0.5&0\\0.5&0&0\\0&0&0\end{bmatrix}. \tag{12}$$

According to the obtained stress field results, the average stress is calculated, and the effective stiffness matrix is inversely calculated.

In order to verify the rationality of ellipsoidal approximation without considering the influence caused by the second reason mentioned above, an RVE_{sm} containing only three pores is intercepted in the RVE_1 for analysis. The three models on the RVE_{sm} with different grid sizes are shown in Figure 9.

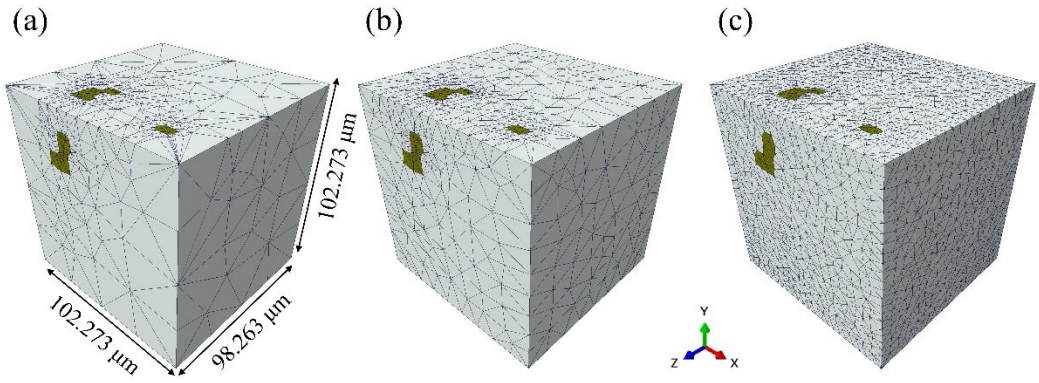

Figure 9 Mesh division of the RVE_{sm}, where (a) low mesh quality, (b) middle mesh quality and (c) high mesh quality.

Table 3 lists the components of the elastic stiffness matrix predicted by FEM and the MT model. It can be seen that the prediction results of FEM and the MT model are very similar, and there are the relations $C_{33}>C_{11}>C_{22}$ and $C_{66}<C_{44}$, C_{55}. The difference on the prediction results between the MT model and FEM decreases with the increase of the grid density.

Table 3 Comparison of the effective stiffness matrix of the RVE_{small} predicted by the MT model and FEM (GPa)

	C_{11}	C_{12}	C_{13}	C_{22}	C_{23}	C_{33}	C_{44}	C_{55}	C_{66}
(a)	91.286	7.405	7.393	90.592	7.423	92.013	83.888	84.240	83.440
(b)	90.951	7.472	7.403	90.678	7.486	91.755	83.734	83.929	83.199
(c)	90.677	7.502	7.411	90.427	7.514	91.488	83.422	83.620	82.865
MT	89.942	7.164	7.538	89.918	7.468	90.724	82.607	82.529	81.287

Figure 10 shows the Mises stress of the RVE_{sm} under ε_1 (tension along X-axis), where half of the length on the RVE_{sm} along the X-axis is truncated to observe the stress distribution around

the pores. It can be seen from Figure 10 that, the stress in the pore is obviously less than that in the matrix, and there is a stress disturbance caused by the pores in the matrix around the pore. It can be seen from the local figures that, this stress disturbance becomes obvious with the increase of the grid density and tends to be more practical. With the improvement of the grid quality, the prediction results of effective moduli becomes smaller, which shows that the variation range of the low stress area of matrix is higher than that of the high stress area. In the MT model, this disturbance is averaged to the whole matrix region, so the effective moduli predicted by the MT model is more suitable for the case of inclusions with large volume fraction than the sparse model or the Kuster-Toksöz model. By comprising the results between the MT model and FEM in Table 3, it can be seen that the averaging treatment of stress disturbance in the MT model is reasonable in predicting the effective moduli.

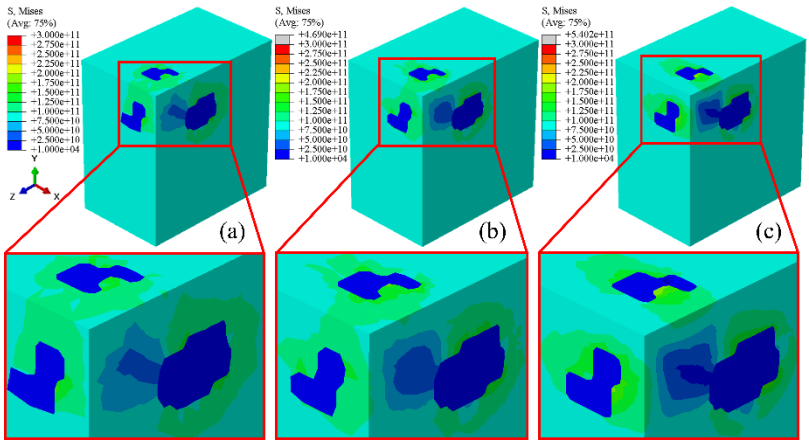

Figure 10 Mises stress of the RVE_{sm} under tension along *X*-axis

Further, the three kinds of RVE_1 with different grid densities are analyzed by FEM, of which the grid division is shown in Figures 11 (a), (b) and (c). There are 8599, 49565, 585803 elements representing the matrix and 3855, 9686, 37346 elements representing the pores in the

three models, respectively. Figures 11 (d), (e) and (f) shows that the Mises stress of RVE_1 under ε_1 (tension along X-axis), where we cut the half of RVE_1 to observe the stress distribution. Similar to the analysis results of RVE_{sm}, the stress disturbance area of the matrix around the pores gradually increases with the densification of the grid, and the effective moduli of RVE_1 generally decreases slightly with the densification of the grid, which can be seen from Table 4. It can be seen that the anisotropy laws of RVE1 predicted by FEM is in agreement with that by the MT model, i.e., $C_{11} > C_{22} > C_{33}$ and $C_{44} < C_{55} < C_{66}$. Therefore, in the RVE_1, the secondd reason mentioned above has little effect on the anisotropy.

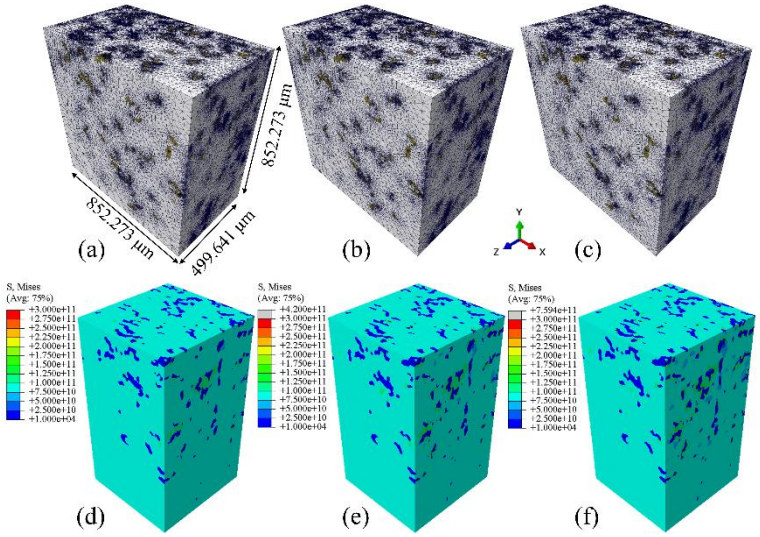

Figure 11 Mesh division and Mises stress of the RVE, where (a), (b) and (c) are the low, middle and high mesh quality, and (d), (e) and (f) are the corresponding Mises stress under tension along X-axis.

However, comparing the results between Table 3 and 4, it can be found that the difference between the results of RVE_1 predicted by FEM and the MT model is larger than that of the RVE_{sm}. The main reason is that the volume ratio between the pore and element in RVE1 is

smaller than that in RVE_{sm}, and there are relatively large errors on the matrix stress disturbance near the pores. However, further refinement of the grid will greatly affect the computational efficiency of FEM and put forward high requirements for the running memory of the computer.

Table 4 Comparison of the effective stiffness matrix of RVE_1 predicted by the MT model and FEM (GPa)

	C_{11}	C_{12}	C_{13}	C_{22}	C_{23}	C_{33}	C_{44}	C_{55}	C_{66}
(a)	90.595	7.269	7.207	90.077	7.195	89.005	82.224	82.503	83.040
(b)	88.974	7.187	7.097	88.209	7.096	86.450	79.989	80.448	81.348
(c)	87.941	7.184	7.079	86.974	7.105	84.701	78.353	78.978	80.170
MT	86.973	7.342	7.309	85.606	7.468	83.137	77.613	77.706	78.940

4.3 Effect of the volume fraction of inclusions

In what follows, the effective moduli of the RVE_1 to RVE_{36} containing the quartz/matrix and pores/inclusions are predicted by the MT model and FEM for analyzing the effect of inclusion's volume fraction. One of the reasons that the MT model can be widely used is that, it can be applied to the case dealing with a large volume fraction of inclusions (Raju et al., 2018). The effective moduli of the RVE_1 to RVE_{36} predicted by the MT model and FEM are shown in Figure 12 and the average values are shown in Table 5.

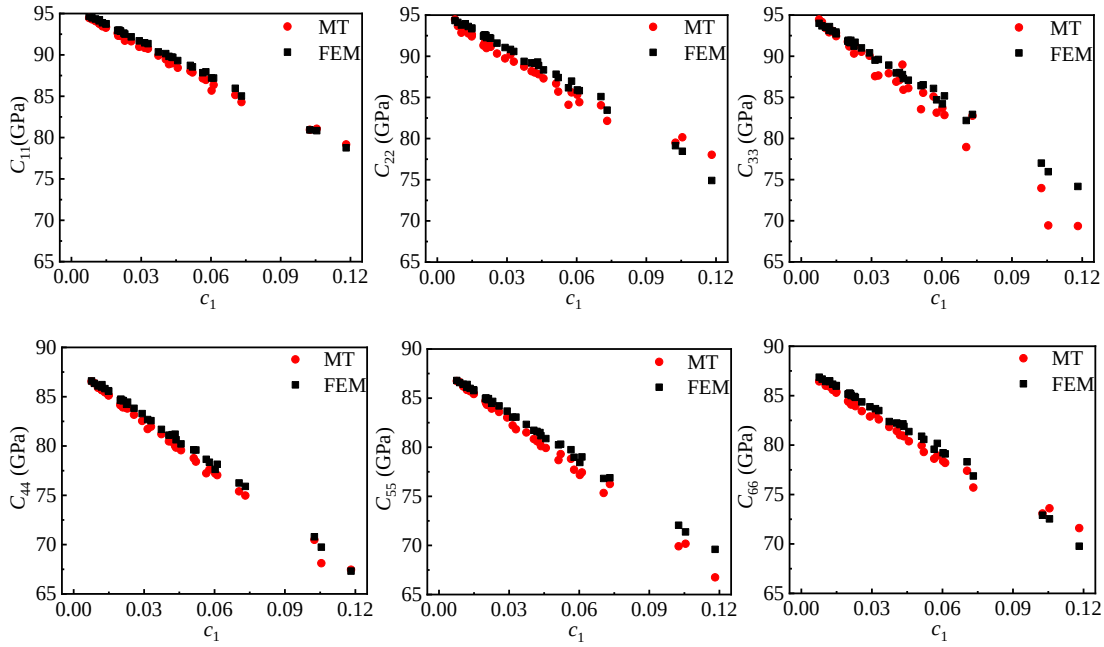

Figure 12 Relationship between components of effective elastic stiffness matrix and volume fraction of pores.

Table 5 Average effective stiffness matrix of RVE_1 to RVE_{36} predicted by the MT model and FEM (GPa)

	C_{11}	C_{12}	C_{13}	C_{22}	C_{23}	C_{33}	C_{44}	C_{55}	C_{66}
MT	89.675	7.444	7.483	88.533	7.502	87.228	40.385	82.503	83.040
FEM	90.215	7.337	7.269	89.354	7.281	88.378	40.701	80.448	81.348

The prediction results of the two methods are close, and the laws of anisotropy are same, which are $C_{11} > C_{22} > C_{33}$ and $C_{44} < C_{55} < C_{66}$. Moreover, the effective moduli predicted by the two methods decrease linearly with the increase of volume fraction of inclusions. In fact, it can be seen from previous studies that, when the shape of the inclusions is not a disk shape ($\bar{a}_2 / \bar{a}_1 \to 1$, $\bar{a}_3 / \bar{a}_1 \ll 1$), the relationship between the effective moduli preidcted by the MT model and volume fraction of the inclusions basically changes linearly (Wang et al., 2021). It

is very interesting that the results predicted by the MT model is more discrete than that of FEM, especially when the inclusion volume fraction is large, which indicates that the MT model may overestimate the influence of inclusion's orientation on the anisotropy of the RVE. However, when using the digital core for modeling, in FEM we have to calculate a large number of elements and its efficiency is relatively low. Therefore, the combination of the MT model and digital core proves a practical and efficient method to predict the anisotropy of shales and other kinds of rock.

5 Discussion

The combination of MT model and digital core technology has guiding significance for the development of effective medium model. For the traditional effecitve medium models based on the Eshelby tensor, such as KT model (Kuster & Toksöz, 1974), self consistent model (Hill, 1965) and different effective medium model (Xu & White, 1995), the aspect ratio α of rotating ellipsoid inclusions, or the shape of ellipsoid, plays a key role in the evaluation of effective moduli. The α is assumed in the previous theoretical analyses, and it seems to be considered that can be reflect the shape of inclusions. However, it can be seen from Figure 6 that the shape of inclusions in shale sample is more like general ellipsoid than rotating ellipsoid from the average pricipal radii of inclusions extracted by micro-CT and moment of inertia. Therefore, in order to obtain more accurate elastic properties, the Eshelby tensor of general ellipsoid should be used for evaluation. In addition, we confirmed the similar laws in previous studies (Sayers, 1994; Vernik and Landis, 1996; Giraud et al., 2007) that the the orientation of inclusions in shale is regular, which can be seem in Figures 7 and 8.

The elastic stiffness matrix of shale samples is predicted by MT model in Tab 2 and it can be found that there is still some anisotropy in shale with micro scale. For verify the accurancy of MT model when predicting the anisotropy of shale, a series of squartz-pore mateirals are analyzed by MT model and finite element method (FEM). It can be obviously observed the stress disturbance of the inclusion to matrix assumed in MT model (Mori and Tanaka, 1974) from the stress nephogram of FEM in Figures 10 and 11. And the results of the anisotrpy good agreement between the MT model and FEM which are shown in Tabs 3 to 5. Therefore, micro-CT provide proper information regarding non-randomly oriented inclusions in shale, and thereby aids in the utilization of the MT model.

6 Conclusions

In the present study, we establish and verify a prediction method for anisotropic effective moduli of Longmaxi formation shales based on the digital core, the Mori-Tanaka (MT) model and the finite element method (FEM). We find that the moment of inertia of incluisons in shales can be used to obtain the principal radius and Eulerian angles of its representative ellipsoid. By analyzing the shale components extracted by digital core, it is found that the orientation distribution of different components in the shale is similar to the theoretical function given by Giraud. (1) The orientation distribution of pores, TOC and clay has a strong anisotropy by fitting the orientation distribution function. The geometry of pores is close to that of TOC, while that of clay, feldspar and pyrite is close. (2) The effective elastic stiffness matrix of representative volume element (RVE) of shale samples is obtained by the MT model considering the shape and orientation of inclusions. Through the five groups of two-phase

material models, it is determined that pores, TOC and clay contribute greatly to the anisotropy of shale, and feldspar and pyrite hardly affect the anisotropy of shale samples. (3) The effective ealstic stiffness matrixs of multiple groups of quartz-pore RVE obtained by the digital core are predicted by the MT model and FEM, and the anisotropy of RVE predicted by the two methods is consistent. The effective moduli changes linearly with the inclusion volume fraction, and the discrete prediction result of MT is greater than that of FEM. These findings are potential for the applications in rock mechanics, civil engineering and oil exploitation, etc.

Acknowledgements

The authors greatly appreciate the financial support of the Strategic Priority Research Program of the Chinese Academy of Sciences (XDA14010303), the National Natural Science Foundation of China (11972375, 11911530691), and Key R & D Program in Shandong Province (ZR202011050038, 2017GGX20117).

Data Availability Statement

The supporting information involved in this study is available within this article.

Appendix A

The three most typical components of the Hill tensor $\boldsymbol{P}$ on the general ellipsoid in the local coordinate system O-$x_1x_2x_3$ can be expressed as

$$\left.\begin{aligned} P_{1111} &= \frac{3a_1^2}{16\pi G_0(1-\nu_0)}W_{11} + \frac{1-4\nu_0}{16\pi G_0(1-\nu_0)}W_1 \\ P_{1212} &= \frac{1}{16\pi G_0(1-\nu_0)}\left(a_1^2 W_{12} + W_1\right) - \frac{\nu_0}{16\pi G_0(1-\nu_0)}\left(W_1 + W_2\right) \\ P_{1122} &= \frac{a_1^2}{16\pi G_0(1-\nu_0)}W_{12} - \frac{1}{16\pi G_0(1-\nu_0)}W_2 \end{aligned}\right\}, \tag{A1}$$

and the other components can be obtained by the corner mark rotation, such as

$$\left.\begin{aligned} P_{3232} &= \frac{1}{16\pi G_0(1-\nu_0)}\left(a_3^2 W_{32} + W_3\right) - \frac{\nu_0}{16\pi G_0(1-\nu_0)}\left(W_3 + W_2\right) \\ P_{3322} &= \frac{a_3^2}{16\pi G_0(1-\nu_0)}W_{32} - \frac{1}{16\pi G_0(1-\nu_0)}W_2 \end{aligned}\right\}. \tag{A2}$$

In addition, the tensor of $\boldsymbol{P}$ has the symmetry of $P_{ijkl} = P_{jikl} = P_{ijlk} = P_{klij}$. In Equations (A1) and (A2), there are

$$\left.\begin{aligned} W_{12} &= W_{21} = \frac{W_2 - W_1}{a_1^2 - a_2^2},\ W_{13} = W_{31} = \frac{W_3 - W_1}{a_1^2 - a_3^2},\ W_{23} = W_{32} = \frac{W_3 - W_1}{a_2^2 - a_3^2} \\ W_{11} &= \frac{4\pi}{3a_1^2} - \frac{1}{3}\left(W_{12} + W_{13}\right),\ W_{22} = \frac{4\pi}{3a_2^2} - \frac{1}{3}\left(W_{12} + W_{23}\right) \\ W_{33} &= \frac{4\pi}{3a_3^2} - \frac{1}{3}\left(W_{13} + W_{23}\right) \end{aligned}\right\}, \tag{A3}$$

where

$$\left.\begin{aligned} W_1 &= \frac{4\pi a_1 a_2 a_3}{\left(a_1^2-a_2^2\right)\sqrt{a_1^2-a_3^2}}\left[F\left(\xi,\zeta\right)-E\left(\xi,\zeta\right)\right] \\ W_2 &= 4\pi a_1 a_2 a_3\left[\frac{\sqrt{a_1^2-a_3^2}}{\left(a_2^2-a_3^2\right)\left(a_1^2-a_2^2\right)}E\left(\xi,\zeta\right)\right. \\ &\quad \left.-\frac{F\left(\xi,\zeta\right)}{\left(a_1^2-a_2^2\right)\sqrt{a_1^2-a_3^2}}-\frac{a_3}{a_1 a_2\left(a_2^2-a_3^2\right)}\right] \\ W_3 &= \frac{4\pi a_1 a_2 a_3}{\left(a_2^2-a_3^2\right)\sqrt{a_1^2-a_3^2}}-\left[\frac{a_2\sqrt{a_1^2-a_3^2}}{a_1 a_3}\right]-E\left(\xi,\zeta\right) \end{aligned}\right\}, \tag{A4}$$

The symbols $F(\xi,\zeta)$ and $E(\xi,\zeta)$ are the elliptic integrals of type I and type II, respectively, which are

$$\left.\begin{aligned} F\left(\xi,\zeta\right) &= \int_0^{\xi}\frac{\mathrm{d}y}{\sqrt{1-\zeta^2\sin^2 y}} \\ E\left(\xi,\zeta\right) &= \int_0^{\xi}\sqrt{1-\zeta^2\sin^2 y}\,\mathrm{d}y \end{aligned}\right\}, \tag{A5}$$

where $\xi=\arcsin\sqrt{1-\left(a_3/a_1\right)^2}$ and $\zeta=\sqrt{\left(a_1^2-a_2^2\right)/\left(a_1^2-a_3^2\right)}$.

Appendix B

The coordinates of the geometric center of the inclusion domain Ω in the coordinate system *O-XYZ* are

$$M_X=\frac{1}{V_\Omega}\int_\Omega X\mathrm{d}X\mathrm{d}Y\mathrm{d}Z,\quad M_Y=\frac{1}{V_\Omega}\int_\Omega Y\mathrm{d}X\mathrm{d}Y\mathrm{d}Z,\quad M_Z=\frac{1}{V_\Omega}\int_\Omega Z\mathrm{d}X\mathrm{d}Y\mathrm{d}Z, \tag{B1}$$

where M_X, M_Y, M_Z are the coordinate values of the geometric center of inclusion domain Ω in *O-XYZ*, and V_Ω is the volume of inclusion domain. Then, the components of the inertia matrix of the inclusion domain are

$$M_{2X} = \frac{1}{V_\Omega}\int_\Omega \left(X - M_X\right)^2 \mathrm{d}X\mathrm{d}Y\mathrm{d}Z \,,$$

$$M_{2Y} = \frac{1}{V_\Omega}\int_\Omega \left(Y - M_Y\right)^2 \mathrm{d}X\mathrm{d}Y\mathrm{d}Z \,,$$

$$M_{2Z} = \frac{1}{V_\Omega}\int_\Omega \left(Z - M_Z\right)^2 \mathrm{d}X\mathrm{d}Y\mathrm{d}Z \,,$$

(B2)

$$M_{2XY} = \frac{1}{V_\Omega}\int_\Omega \left(X - M_X\right)\left(Y - M_Y\right) \mathrm{d}X\mathrm{d}Y\mathrm{d}Z \,,$$

$$M_{2YZ} = \frac{1}{V_\Omega}\int_\Omega \left(Y - M_Y\right)\left(Z - M_Z\right) \mathrm{d}X\mathrm{d}Y\mathrm{d}Z \,,$$

$$M_{2ZX} = \frac{1}{V_\Omega}\int_\Omega \left(Z - M_Z\right)\left(X - M_X\right) \mathrm{d}X\mathrm{d}Y\mathrm{d}Z \,.$$

References:

Berryman, J.G., 1995. *Mixture Theories for Rock Properties*. Elseveier.

Cheng, C.H., 1993. Crack models for a transversely isotropic medium, *Journal of Geophysical Research: Solid Earth*, **98**, 675–684. https://doi.org/10.1029/92JB02118

David, E.C., Zimmerman, R.W., 2011. Compressibility and shear compliance of spheroidal pores: Exact derivation via the Eshelby tensor, and asymptotic expressions in limiting cases, *International Journal of Solids and Structures*, **48**, 680–686. https://doi.org/10.1016/j.ijsolstr.2010.11.001

David, E.C., Zimmerman, R.W., 2011. Elastic moduli of solids containing spheroidal pores, International Journal of Engineering Science, **49**, 544–560. https://doi.org/10.1016/j.ijengsci.2011.02.001

Deng, J.X., Zhou, H., Wang, H., Zhao, J.G. & Wang, S.X., 2015. The influence of pore structure in reservoir sandstone on dispersion properties of elastic waves, *Chinese Journal of Geophysics*, **58**, 3389–3400 (in Chinese). https://doi.org/10.6038/cjg20150931

Drach, B., Drach, A. & Tsukrov, I., 2013. Characterization and statistical modeling of irregular porosity in carbon/carbon composites based on X-ray microtomography data, *ZAMM-Zeitschrift fur Angewandte Mathematik und Mechanik*, **93**, 346–366. https://doi.org/10.1002/zamm.201100190

Drach, B., Tsukrov, I., Gross, T., Dietrich, S., Weidenmann, K., Piat, R. & Bohlke, T., 2011. Numerical modeling of carbon/carbon composites with nanotextured matrix and 3D pores of irregular shapes, *International Journal of Solids and Structures*, **48**, 2447–2457. https://doi.org/10.1016/j.ijsolstr.2011.04.021

Eshelby J.D., 1957. The determination of the elastic field of an ellipsoidal inclusions, and related problems, *Proceedings of the Royal Society of London, Series A: Mathematical and*

Physical Sciences, **241**, 376–396.

Giraud, A., Huynh, Q.V., Hoxha, D. & Kondo D., 2007. Effective poroelastic properties oftransversely isotropic rock-like composites with arbitrarily oriented ellipsoidal inclusions, *Mechanics of Materials*, **39**, 1006–1024. https://doi.org/10.1016/j.mechmat.2007.05.005

Goodarzi, M., Rouainia, M. & Aplin, A.C., 2016. Numerical evaluation of mean-field homogenization methods for predicting shale elastic response, *Computers and Geosciences*, **20**, 1109–1122. https://doi.org/10.1007/s10596-016-9579-y

Gui, J.C., Ma, T.S., Chen, P., Yuan, H. & Guo, Z., 2018. Anisotropic damage to hard brittle with stress and hydration coupling, *Energies*, **11**, 926. https://doi.org/10.3390/en11040926

Hill, R., 1965. A self-consistent mechanics of composite materials, *Journal of the Mechanics and Physics of solids*, **13**, 213–222. https://doi.org/10.1016/0022-5096(65)90010-4

Hudson, J.A., 1986. A higher order approximation to the wave propagation constants for a cracked solid, *Geophysical Journal of the Royal Astronomical Society*, **87**, 265–274. https://doi.org/10.1111/j.1365-246X.1986.tb04556.x

Jian, S.K., Fu, L.Y., Wang, Z.W., Han, T.C. & Liu, J.L., 2020. Elastic equivalent numerical modeling based on the dynamic method of Longmaxi Formation shale digital core, *Chinses Journal of Geophysics*, **63**, 2786–2799 (in Chinese).

Mavko, G., Mukerji, T. & Dvorkin, J., 1998. *The Rock Physics Handbook: Tools for Seismic Analysis of Porous Media*. Cambridge University Press.

Moon, J., Yoon, S. & Monteiro P.J., 2015. Mechanical properties of jennite: a theoretical and experimental study, *Cement and Concrete Research*, **71**, 106–114. https://doi.org/10.1016/j.cemconres.2015.02.005

Mori, T. & Tanaka, K., 1974. Average stress in matrix and average elastic energy of materials with misfitting inclusions, *Acta Metallurgica*, **21**, 571–574. https://doi.org/10.1016/0001-

6160(73)90064-3

Park, I., Moon, J., Bae, S., Oh, J.E. & Yoon, S., 2020. Application of micro-CT to Mori-Tanaka method for non-randomly oriented pores in air-entrained cement pastes, *Construction and Building Materials*, **255**, https://doi.org/119342.10.1016/j.conbuildmat.2020.119342

Prasad, M., Pal–Bathija, A., Johnston M., Rydzy, M. & Batzle, M., 2009. Rock physics of the unconventional, *Geophysics: the leading edge of exploration*, **28**, 34–38.

Raju, B., Hiremath, S.R, Roy Mahapatra, D., 2018. A review of micromechanics based models for effective elastic properties of reinforced polymer matrix composites, *Composite Structure*, **204**, 607–619. https://doi.org/10.1016/j.compstruct.2018.07.125

Sahimi, M. & Tahmasebi, P., 2021. Reconstruction, optimization, and design of heterogeneous mateirals and media: Basic principles, computational algorithms, and applications, *Physics Reports*, **939**, 1–82.

Sayers, C.M., 1994. The elastic anisotropy of shales, *Journal of Geophysical Research: Solid Earth*, **99**, 767–774.

Shapiro, S.A. & Kaselow, A, 2005. Porosity and elastic anisotropy of rocks under tectonic stress and pore-pressure changes, *Geophysics*, **70**, N27–N28. https://doi.org/10.1190/1.2073884

Shen, G.L., Hu, G.K. & Liu, B., 2013. *Mechanics of Composite Materials*. Tsinghua University Press (in Chinese).

Shen, H.S., Wang, Z.X., 2012. Assessment of voigt and Mori-Tanaka models for vibration analysis of functionally graded plates, *Composite Structures*, **94**, 2197–2208. https://doi.org/10.1016/j.compstruct.2012.02.018

Thomsen, L., 1986. Weak elastic anisotropy, Geophysics, **51**, 1954–1966. 10.1190/1.1442051

Vernik, L. & Nur, A., 1992. Petrophysical analysis of the Cajon Pass scientific well:

Implications for fluid flow and seismic studies in the continental crust, *Journal of Geophysical Research: Solid Earth*, **97**, 5121–5134. https://doi.org/10.1029/91JB01672

Vernik, L. & Landis, C, 1996. Elastic anisotropy of source rocks: Implications for hydrocarbon generation and primary migration, *AAPG Bull.*, **80**, 531–544. https://doi.org/10.1016/j.revinf.2014.12.016

Wang, J.F., Zhang, L.W., Liew, K.W., 2017. Multiscale simulation of mechanical properties and microstructure of CNT-reinforced cement-based composites, *Computer Methods in Applied Mechanics and Engineering*, **319 (Supplement C)**: 393–413. https://doi.org/10.1016/j.cma.2017.02.026

Wang, Z.D., Zhang, Q., Liu, J.L. & Fu, L.Y., 2021. Effective moduli of rocks predicted by the Kuster-Toksöz and Mori-Tanaka models, *Journal of Geophysics and Engineering*, **18**, 539–557. https://doi.org/10.1093/jge/gxab034

Xu, S. & White, R. E., 1995. A new velocity model for clay-sand mixtures, *Geophysical Prospecting*, **43**, 91–118.

Zhang, Q.G., Fan, X.Y., Chen, P., Ma, T.S. & Zeng, F.T., 2020. Geomechanical behaviors of shale after water absorption considering the combined effect of anisotropy and hydration, *Engineering Geology*, **269**, 105547. https://doi.org/10.1016/j.enggeo.2020.105547

Zhao, J.P., Chen, H., Li, N., Ding, J.L. & Gao, J.S., 2020. Research advance f petrophysical application based on digital core technology, *Progress in Geophysics*, 35, 1099–1198 (in Chinese).

Zhao, J.Z., Zhang, D.X., Wu, T.H., Tang, H.Y., Xuan, Q.H., Jiang, Z. & Dai, Cheng, 2019. Multiscale approach for mechanical characterization of organic-rich shale and its application, International Journal of Geomechanics, 19, 4018180. https://doi.org/10.1061/(asce)gm.1943-5622.0001281

Zhu, L.Q., Zhang, C., Zhang, C.M., Zhou, X.Q., Zhang, Z.S., Nie, X., Liu, W.N. & Zhu, B.Y., 2019. Challenges and Prospects of Digital Core-Reconstruction Research, Geofluids, 7814180. https://doi.org/10.1155/2019/7814180

Zimmerman, R.W., 1991. Elastic moduli of a solid containing spherical inclusions, *Mechanics of Materials*, **12**, 17–24. https://doi.org/10.1016/0167-6636(91)90049-6